Nanoscale

PAPER

View Article Online
View Journal | View Issue

Cite this: *Nanoscale*, 2020, **12**, 20326

Membrane poration, wrinkling, and compression: deformations of lipid vesicles induced by amphiphilic Janus nanoparticles†

Jared T. Wiemann, ‡[a] Zhiqiang Shen, ‡[b] Huilin Ye, [b] Ying Li *[c] and Yan Yu *[a]

Received 20th July 2020,
Accepted 24th September 2020

DOI: 10.1039/d0nr05355d

rsc.li/nanoscale

Building upon our previous studies on interactions of amphiphilic Janus nanoparticles with glass-supported lipid bilayers, we study here how these Janus nanoparticles perturb the structural integrity and induce shape instabilities of membranes of giant unilamellar vesicles (GUVs). We show that 100 nm amphiphilic Janus nanoparticles disrupt GUV membranes at a threshold particle concentration similar to that in supported lipid bilayers, but cause drastically different membrane deformations, including membrane wrinkling, protrusion, poration, and even collapse of entire vesicles. By combining experiments with molecular simulations, we reveal how Janus nanoparticles alter local membrane curvature and collectively compress the membrane to induce shape transformation of vesicles. Our study demonstrates that amphiphilic Janus nanoparticles disrupt vesicle membranes differently and more effectively than uniform amphiphilic particles.

Introduction

It is well recognized that the surface chemistry of nanoparticles is a key factor in determining their potential cytotoxicity, especially the potentially adverse impact on biological membranes.[1–4] Studies have been extensively focused on nanoparticles with uniform surface coatings. In general, cationic nanoparticles were found to be more disruptive to lipid membranes than anionic particles, in terms of causing defects[5–11] and morphological deformations of membranes[6,12,13] and perturbing membrane fluidity.[14,15] Particle-membrane interactions become more complex when hydrophobicity is present on particle surfaces. The cytotoxicity of amphiphilic particles has been shown to correlate with their degree of hydrophobicity.[7,16,17] These nanoparticles were found to translocate through model lipid membranes[18–21] and erythrocyte plasma membranes,[22] induce pores in model lipid membranes,[23–25] and stabilize open edges of pre-formed membrane defects.[26] Likewise, computer simulations have predicted that amphiphilic particles either become trapped or pass through membranes based on hydrophobicity[27,28] and interrupt lipid packing upon membrane insertion.[20,29] These studies have established a critical foundation for understanding nano-bio interactions. However, one factor that has been overlooked is the surface heterogeneity of nanoparticles.

Some nanoparticles were engineered to have heterogeneous surface compositions for specific applications such as catalysis.[30–32] More often, engineered uniform nanoparticles acquire a non-uniform surface coating during their environmental circulation due to the adsorption of environmental contaminants.[33,34] Some studies have shown that nanomaterials after surface adsorption of organic pollutants in water become more toxic to aquatic organisms,[34–37] which highlight the important role the surface heterogeneity of nanoparticles might play in determining their cytotoxicity. In cases of particle-membrane interactions, we and other groups have shown that the spatial arrangement of hydrophobic and charged groups on nanoparticles changes their routes of disruption to biological membranes. Experiments and computer simulations have shown that when hydrophobic and hydrophilic ligands are arranged in striped patterns on nanoparticles, it promotes the translocation of nanoparticles through membranes without causing damage,[38–40] even though the experimental confirmation of the striped ligand patterns has been under debate.[41,42] Simulations on amphiphilic Janus nanoparticles, particles that are hydrophobic on

[a]*Department of Chemistry, Indiana University, Bloomington, Indiana 47405, USA. E-mail: yy33@indiana.edu*
[b]*Department of Mechanical Engineering, University of Connecticut, Storrs, Connecticut 06269, USA*
[c]*Department of Mechanical Engineering and Polymer Program, Institute of Materials Science, University of Connecticut, Storrs, Connecticut 06269, USA. E-mail: yingli@engr.uconn.edu*

†Electronic supplementary information (ESI) available. See DOI: 10.1039/d0nr05355d

‡These authors contributed equally.

one side and charged on the other, have shown that these particles insert into lipid membranes[43] and stabilize membrane edges.[44] Our group studied experimentally the interactions of amphiphilic nanoparticles and planar supported lipid bilayers and systematically examined the role of particle hydrophobicity, particle charge, ligand organization, and lipid bilayer compositions.[45–47] We showed that amphiphilic Janus particles induce defects in glass-supported lipid bilayers more effectively than uniformly amphiphilic particles, regardless of the charges (cationic *vs.* anionic) on the one hemisphere of particles or charges of the lipid membranes.[45,46] We further demonstrated the quantitative relationship between the particle-induced bilayer disruption and the particle hydrophobicity, characterized by the lipophilic balance of the particles.[47]

Based on our previous findings, the goal of our present study is to understand the impact of amphiphilic Janus nanoparticles on giant unilamellar vesicle (GUV) membranes, which is a better mimic of cell plasma membranes than planar glass-supported bilayers. We hypothesize that Janus nanoparticles influence the GUV membranes differently based on two considerations: the absence of a solid substrate underneath the bilayer, and the constraints of volume and surface area in GUVs. To test the hypothesis, we integrated experiments with coarse-grained molecular simulations to study the effect of 100 nm amphiphilic Janus nanoparticles, one hemisphere hydrophobic and the other positively charged, on the membrane integrity and morphology of giant unilamellar vesicles (GUVs) consisted of the zwitterionic lipid 1,2-dioleoyl-*sn*-glycerol-3-phosphocholine (DOPC). We found that Janus nanoparticles beyond a threshold concentration of 20 pM lead to a few morphological defects in GUV membranes, including increased local membrane curvature in the form of membrane "wrinkling" and membrane protrusions, and collapse of entire vesicles in some cases. As the GUV membranes deformed upon interactions with the Janus nanoparticles, they also became leaky in a manner that is dependent on the particle concentration. Combining fluorescence lifetime imaging with coarse-grained molecular simulations, we revealed that amphiphilic Janus nanoparticles inserted into membranes, which resulted in more disordered lipid packing and caused local membrane curvature in order to wrap their hydrophobic hemispheres with lipids. The collective effects from multiple particles on a GUV leads to compression and "wrinkling" of membranes.

Materials and methods

Materials and reagents

Amine-functionalized silica nanoparticles (+UNP, 100 nm in diameter) were purchased from NanoComposix (San Diego, CA, USA). Chromium (99.99% purity) and gold (99.99% purity) for particle fabrication were obtained from Kurt J. Lesker, Co. (Jefferson Hills, PA, USA). Octadecane-1-thiol, HEPES, octadecyltrimethoxysilane, and 5(6)-carboxyfluorescein were purchased from Sigma-Aldrich (St Louis, MO, USA). 1,2-Dioleoyl-*sn-glycero*-3-phosphocholine (DOPC), 1,2-dioleoyl-*sn-glycero*-3-phosphoethanolamine-*N*-(lissamine rhodamine B sulfonyl) (RhB-DOPE), and 1-palmitoyl-2-{6-[(7-nitro-2-1,3-benzoxadiazol-4-yl)amino]hexanoyl}-*sn-glycero*-3-phosphocholine (C6-NBD-PC) were from Avanti Polar Lipids, Inc. (Alabaster, AL, USA). ITO-coated slides were purchased from Delta Technologies, Ltd (Loveland, CO). Ultrapure water (18.2 MΩ cm) was used in all experiments.

Nanoparticle fabrication and characterization

Amphiphilic cationic Janus nanoparticles (+/pho JPs) were fabricated as described previously.[46] Briefly, a sub-monolayer of 100 nm cationic silica nanoparticles (+UNPs) was coated on microscope slides that had been cleaned in piranha solution. Thin layers of chromium (5 nm) and gold (25 nm) were sequentially coated onto one hemisphere of the particles using an Edwards thermal evaporation system (Nanoscale Characterization Facility at Indiana University). To make the gold caps on particles hydrophobic, particle monolayers after metal evaporation were immediately immersed in 2 mM 1-octadecanethiol in ethanol for a minimum of 12 h before use. The resulted +/pho JPs were sonicated off the slides within 24 hours prior to use. Particle aggregates due to metal coating bridging were removed by two steps of differential centrifugation (100*g* four times and then 500*g* four times). To fabricate uniform amphiphilic nanoparticles (+pho UNP), octadecyltrimethoxysilane and 1 M HCl were added dropwise to THF to prepare a solution containing 22 mM octadecyltrimethoxysilane and 0.6 vol% of HCl. +UNPs were resuspended in 8 : 1 (v/v) hexanes : octadecyltrimethoxysilane solution with vigorous stirring for 1 h at room temperature. The resulted +pho UNPs were washed several times with ethanol and water and stored until use. All particles were washed with 100 mM glucose at least three times before experiments to remove residual ethanol. Hydrodynamic radius and zeta potential of all particles were characterized using a Malvern Zetasizer (Nanoscale Characterization Facility at Indiana University). Particle gold coating was assessed by scanning electron microscopy (Nanoscale Characterization Facility at Indiana University). Concentration of particles was measured using Particle Metrix ZetaView (Nanoscale Characterization Facility at Indiana University).

GUV electroformation

DOPC and RhB-DOPE were mixed 500 : 1 (mol : mol) in chloroform to prepare stock lipid solution. Approximately 10 μL of lipid stock solution (5.0 mg mL^{-1}) was spread onto an ITO-coated glass slide to make a lipid film. Lipids were dried under nitrogen for at least 30 minutes to remove residual chloroform. 100 mM aqueous sucrose solution was added to the dried lipid film. The lipid coated ITO slide was immediately assembled with another ITO slide and a silicone spacer (1.7 mm thick) into an electroformation chamber. Vesicles were electroformed for 1–2 h under a sinusoidal AC field (3.4 V_{rms}, 5 Hz). GUVs were used within two hours after electroformation.

GUV dye influx

To assess pore formation, GUVs were first suspended in 100 mM aqueous glucose solution containing 25 μM carboxyfluorescein and 0.33 mM HEPES, and then incubated with particles at varied particle concentrations for one hour before imaging. Images were acquired on a Leica SP8 laser scanning confocal microscope with a 63×/1.2 NA water objective. Carboxyfluorescein was excited at 495 nm and its fluorescence was detected between 505–550 nm. At least 20 frames were collected for each sample and a minimum of 45 vesicles were counted for analysis. Each sample was replicated on different days to ensure reproducibility. To count GUVs with poration, the mean fluorescence intensity of carboxyfluorescein inside 100 vesicles in the absence of nanoparticles was first measured. A threshold intensity was defined as three standard deviations greater than the mean. GUVs of which the interior fluorescence intensity was higher than the threshold were counted as GUVs with pore formation.

Fluorescence lifetime imaging of C6-NBD-PC

GUVs electroformed from lipid mixtures with molar ratios of 99 : 1 DOPC : C6-NBD-PC were used for fluorescence lifetime experiments. GUVs were diluted in 100 mM glucose, which helps vesicles to settle to bottom of imaging chambers, prior to imaging. Particles were incubated with vesicles for at least 30 minutes before image acquisition. Fluorescence lifetime images were acquired using a Picoquant PicoHarp 300 time-correlated single photon counting processor on a Leica SP8 laser confocal microscope with a Leica 63×/1.2 NA water objective. C6-NBD-PC was excited using a pulsed white light laser tuned to 470 nm with 20 MHz pulse frequency. Photons with wavelength between 480–700 nm were detected with single photon resolution using a Leica Hybrid Detector. The field of view was limited to include a single vesicle in each image. To acquire enough photons to accurately extract fluorescence lifetimes from photon decay curves, photons were collected until the brightest pixel in the acquisition frame had accumulated 1000 photon counts. Images were analyzed using software SymPhoTime 64. Analyzed regions of the vesicle were separated by areas with particle association and areas without particle association based on fluorescence images. Photon decay curves were fit using the following equation:

$$y = \alpha_1 e^{-t/\tau 1} + \alpha_2 e^{-t/\tau 2}$$

where α_i are pre-exponential factors and τ_i are fluorescence lifetimes. This bi-exponential function has been previously used for C6-NBD-PC in homogeneous DOPC GUVs.[48] Quality of fit was assessed by curve fitting parameter χ^2, and only decay curves with χ^2 between 0.9–1.3 were deemed acceptable. The lifetime component τ_2, which is around 7 ns and known to be sensitive to membrane hydration, was obtained and used in our analysis.

MARTINI simulations

The MARTINI CG force field is adopted in our work to investigate the interaction of the planar lipid bilayer to the Janus nanoparticles. In the MARTINI force field, three or four heavy atoms are treated as one CG interactive bead.[49,50] The MARTINI force field has been proved particularly suitable for studying biomolecular systems. The conformation, dynamics, mechanical properties, and free energy profile of different lipids and molecular species can be correctly reproduced by the MARTINI force field in the CG molecular dynamics simulations.[51] It has been widely applied for investigating problems related to nanoparticle–nanoparticle and nanoparticle–lipid membrane interactions.[29,52,53] In the standard MARTINI CG model, four main types of interaction sites are provided: polar (P), nonpolar (N), apolar (C), and charged (Q).

The model of the AuNPs used in our simulations is adopted from ref. 7, which could reproduce the structure and dynamic properties of the Au core in experimental studies. The Au core of the NP is cut out of a bulk FCC lattice with a constant of 0.408 nm. The size of the gold core is chosen based on the consideration of the balance between computational efficiency and accuracy. If the size of gold core is exactly the one in the experiments, it takes an extremely long time to observe the interaction between the Janus particle and the lipid membrane due to the large size. While, if the gold core size is too small, the Janus particle might insert into the lipid bilayer, which interactive mechanism does not reflect the situation for the large size Janus particle. In this work, the diameter of the gold core is 10 nm, which is around twice the thickness of the lipid bilayer. With this size, the Janus particle will not insert into the lipid bilayer due to its small surface curvature. Furthermore, we can observe the interaction between Janus particle and lipid bilayer with reasonable computational cost. On the hydrophilic part of the gold core, its surface is covered with hydrophilic positive charged Q_d bead with an areal density of 2.5 nm^{-2}. On the hydrophobic part of the gold core, its surface is covered with sulfur beads with an area density of 4.7 nm^{-2}. Each sulfur bead is connected with a hydrophobic alkyl chain with four C_1 beads to mimic the octadecane carbon chain.[7] These settings of areal density are equivalent to the ones in the experiments. The planar bilayer is composed of DOPC lipid molecules. Each system in our simulation is neutralized by adding the corresponding number of chloride beads.

Dry MARTINI simulations

Dry MARTINI method is adopted further to explore the interactions between Janus nanoparticles and lipid vesicle. Dry MARTINI is a solvent-free force field. By considering the solvent implicitly, we can push the limit of molecular simulations to investigate a DOPC vesicle with a diameter around 80 nm. All the potential parameters in the dry MARTINI simulation follows the mapping strategy between dry MARTINI and standard MARTINI potential.[54] All other settings are the same as the standard MARTINI simulations.

Simulation protocol

The temperature in all the simulations is controlled at room temperature (300 K). During the interaction between Janus

nanoparticles and the planar lipid bilayer, the pressure within the plane of the bilayer is coupled controlled at zero. The pressure along the out-of-plane direction is independently controlled at 1 bar. In this way, the planar membrane tension in the simulation is ensured to be zero. Periodic boundary conditions are used in all our simulations. Additionally, before the simulations, both the lipid membrane and nanoparticles are first fully relaxed. During the interaction process, the nanoparticles are placed above the membrane at a distance around 12 nm. The time step of all simulations is set as 30 fs. All simulations are performed using the Large-scale Atomic/Molecular Massively Parallel Simulator (LAMMPS) software.[55] The snapshots during the simulation process are rendered by the Visual Molecular Dynamics (VMD) software.[56]

Results and discussion

Membrane pores induced by +/pho JPs

Our previous study has shown that +/pho JPs beyond a threshold particle concentration induce holes in glass-supported lipid bilayers, but it was unclear if the poration was potentially affected by the flatness of the bilayer and the underlying glass support.[45–47] Here, we first sought to investigate if +/pho JPs disrupt the integrity of the membrane of DOPC GUVs by using a dye influx assay. After electroformation of GUVs composed of DOPC and 0.2% RhB-DOPE in 100 mM aqueous sucrose, we added 25 μM carboxyfluorescein to the exterior GUV medium before mixing GUVs with +/pho JPs of varied concentrations. Carboxyfluorescein is a negatively charged fluorophore that is impermeable to an intact lipid membrane,[57] but it diffuses into GUVs upon membrane poration, leading to increased fluorescence intensity inside GUVs (schematically illustrated in Fig. 1a). As shown by the few representative GUVs in Fig. 1b, an increase of carboxyfluorescein fluorescence intensity inside some GUVs was visible within 10 min after the addition of 40 pM +/pho JPs, which indicates pore formation on the GUVs. However, no pores were visualized directly in fluorescence images, suggesting that the pores may be transient or smaller than the spatial resolution of the confocal fluorescence microscopy (~300 nm). The +/pho JPs appeared as dark spots in the images because the gold caps on the particles block the fluorescence emission from the dye-filled background. This allowed us to visualize the presence of particles, even though not sufficient to identify single particles. We observed that the +/pho JPs unbound to GUVs remained dispersed during our experimental time window, but gradually aggregated into multimers over the course of a few hours.

By measuring the fluorescence intensity inside GUVs as a function of time, we found that the poration kinetics is heterogeneous among all GUVs (Fig. 1c). The influx of carboxyfluorescein into GUVs was more rapid in some GUVs than others, and some GUVs never exhibited any dye influx within the observation period of 30 min after the mixing of GUVs with particles. In a fraction of GUVs exhibiting dye influx, the interior fluorescence intensity plateaued without reaching the same intensity level as in the exterior solution, suggesting that pores induced by +/pho JPs may be transient and the vesicle membrane seals over time. This is in contrast to supported

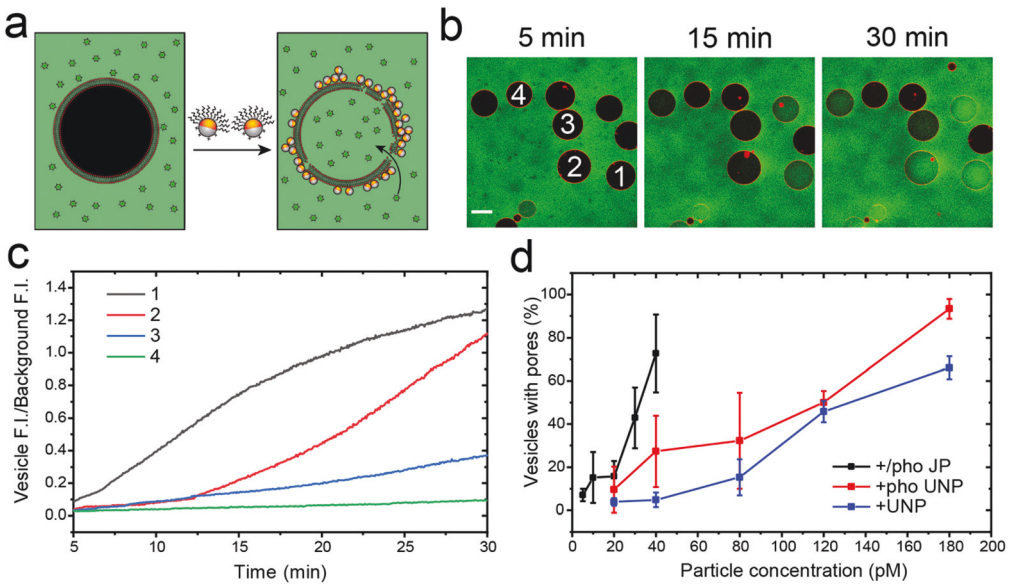

Fig. 1 GUV membrane leakage induced by +/pho JPs. (a) Schematic illustration of the dye influx experiments to probe GUV membrane leakage. (b) Fluorescence images showing GUVs (membrane shown in red) and carboxyfluorescein influx (shown in green) at various time points as indicated in the presence of 40 pM +/pho JPs. (c) Plots showing the fluorescence intensity of carboxyfluorescein inside individual GUVs shown in (b) as a function of time. (d) Fraction of GUVs showing dye influx is plotted as a function of particle concentration for different types of particles: amphiphilic Janus particles (+/pho JPs), amphiphilic uniform particles (+pho UNPs), and cationic uniform particles (+UNPs). Each data point is an average from 50–150 GUVs from three independent samples. Error bars represent one standard deviation. Scale bars: 15 μm.

lipid bilayers where pores do not recover over time.[25,45] We found that the overall percentage of GUVs showing pore formation varied depending on the particle concentration. We imaged GUVs one hour after incubation with +/pho JPs at various concentrations and counted the percentage of GUVs showing influx of carboxyfluorescein. A total of at least 50 GUVs from three independent samples were analyzed. As shown in Fig. 1d, more than 97% of GUVs remained intact and showed no detectable influx of carboxyfluorescein without interaction with +/pho JPs. A slightly larger percentage of GUVs started to show dye influx as the +/pho JP concentration was increased to 20 pM, but that fraction remained low at <20%. However, beyond 20 pM +/pho JPs, the percentage of GUVs with dye influx increased drastically and reached to ~ 80% at 40 pM particle concentration. It is clear from this result that +/pho JPs induce membrane pores in DOPC GUVs in a particle concentration-dependent manner. More importantly, the result shows that a particle concentration of 20 pM or higher is required for inducing extensive membrane disruption. This concentration threshold agrees surprisingly well with our previous finding that +/pho JPs at a concentration of 20 pM or higher were necessary to induce holes in glass-supported DOPC bilayers.[46]

In contrast to the significant vesicle poration induced by +/pho JPs, we observed that particles uniformly coated with only cationic amine groups (referred to as "+ UNP") exert more subtle effects on the GUV membranes (Fig. 1d). Pore formation was induced in a significantly lower percentage of GUVs by +UNPs compared to +/pho JPs at same concentrations. The percentage of GUVs showing dye influx increased gradually with +UNP concentration, but noticeable extent of vesicle poration was only observed after +UNP concentration was increased to about 120 pM, as opposed to 30 pM in the case of +/pho JPs. This result comparison indicates that the particle hydrophobicity plays a major role in driving the vesicle poration.

To further determine the effect of surface heterogeneity, we compared the effect of +/pho JPs *versus* particles uniformly coated with cationic amine groups and hydrophobic alkyl chains (referred to as "+pho UNPs"). We prepared +pho UNPs by functionalizing cationic amine particles with octadecyltrimethoxysilane, an alkylsilane with the same carbon chain length as octadecanethiol on the +/pho JPs. The +pho UNPs after silanization had an average zeta potential of 40 ± 1 mV, compared to 58 ± 1 mV for +UNPs (Fig. S1 of ESI†). This decreased zeta potential reflects the increased hydrophobicity of particles, an observation consistent with previous literature reports.[58,59] After measuring the percentage of GUVs showing dye influx, we found that the +pho UNPs, compared to +UNPs, are more effective in inducing membrane poration in GUVs at all concentrations. This again indicates that the hydrophobicity of nanoparticles is a major driving force in membrane disruption. However, +pho UNPs, despite their amphiphilicity, caused dye influx in a significantly lower percentage of GUVs than +/pho JPs did at same particle concentrations. Only until concentration of +pho UNP was increased to 180 pM did they start to induce the same degree of vesicle poration as observed for 40 pM +/pho JPs. The differential effects of +/pho JPs and +pho UNPs on vesicle poration show that the segregation of cationic and hydrophobic functional groups on particles render them more potent in disrupting vesicle membranes. As we have shown previously that +/pho JPs bind with greater affinity to glass-supported DOPC bilayers than +UNPs and +pho UNPs and hence disrupt membranes at lower bulk particle concentrations,[46] the same mechanism is likely involved in the vesicle-particle interaction. While the presence of glass substrate is a factor that can potentially bias observations in particle-lipid membrane interaction studies, our results so far indicate that +/pho JPs effectively induce pores in the zwitterionic lipid membranes regardless of the presence of underlying glass substrates.

GUV morphological changes

During the dye influx experiments, we observed that a large fraction of GUVs were deformed after incubation with +/pho JPs at 40 pM. We therefore examined GUV morphologies upon interaction with particles using confocal fluorescence microscopy. Particle-induced deformation of GUVs was dependent on +/pho JP concentration, where 40 pM +/pho JPs had the most significant influence. The morphological changes of GUVs can be roughly categorized into three populations: membrane protrusions, invaginations, and collapse of the entire vesicles. The most frequently observed phenomenon was small lipid protrusions (Fig. 2a–d). These protrusions have irregular shapes of a few micrometers in size. They were formed near membrane areas with a relatively high density of adsorbed +/pho JPs, which appeared as dark spots in the fluorescence images. The protrusions were observed to colocalize with the particles, indicating that many of them are complexes formed by excluded lipids and the +/pho JPs (Fig. 2e and more images in Fig. S2†). In some GUVs, the membrane protrusions were concentrated near the bottom half of the vesicles, possibly because the +/pho JPs aggregate on membranes over time and gradually settle (Movie S1†). The second phenomenon observed was membrane invagination in approximately 10% of GUVs. The invaginations, characteristic of high local negative curvatures, appeared alongside of the membrane protrusions in membrane areas of high-density particle binding (Fig. 2e). It is important to note that the blurry, dark spots that appear inside the membrane are in fact from particles that were outside the GUV and out of the imaging focal plane, which we confirmed in scanning along the *z*-axis. In addition to forming membrane protrusion and invagination, less than 5% of the GUVs collapsed into a flat lipid bilayer after interaction with +/pho JPs (Fig. 2f and Movie S2†). We noted that the collapse of a GUV took several minutes to complete. At the end of vesicle rupture, the membrane-bound lipid-particle complexes, as indicated by the intensely fluorescent spots, were found to concentrate in the center of the lipid bilayer (Fig. 2f and Movie S3†). The results clearly demonstrate that the +/pho JPs induce shape deformation of GUVs, in addition to the pore formation. The diverse types of morphological changes are likely a result from the heterogeneous distribution of particles on vesicles.

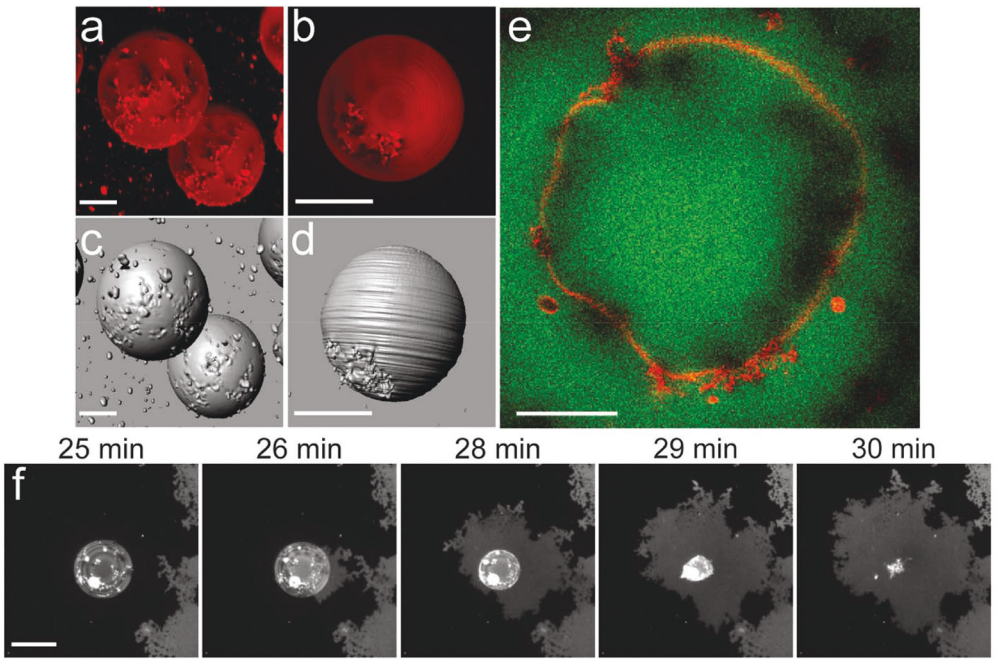

Fig. 2 Morphological changes of GUVs induced by +/pho JPs. Reconstructed 3D (a) and *z*-projection (b) fluorescence confocal microscopy images showing protrusions of GUVs in presence of 40 pM +/pho JPs. (c and d) 3D surface reconstructions of fluorescence confocal microscopy images of the vesicles shown in (a) and (b). (e) A merged fluorescence confocal image showing the local membrane curvature of GUVs in the presence of 40 pM +/pho JPs. GUV membrane is shown in red. Carboxyfluorescein (shown in green) was added in the bulk solution in order to make the particles visible as dark spots. (f) Time-lapse fluorescence confocal images showing the collapse of a GUV in presence of 40 pM +/pho JPs. Scale bars: 20 μm.

Importantly, we found that the asymmetric surface presentation of the amine and hydrophobic groups on Janus particles plays an important role in causing the vesicle shape changes, as we found significantly more protrusions in GUVs upon interaction with 40 pM +/pho JPs compared to those with +pho UNPs even up to 120 pM (Fig. S3†). Consistent with our observation of the induced pore formation, this result indicates that Janus particles are more potent in disrupting vesicle membranes than their uniform particle counterparts.

Disrupted lipid packing

The membrane protrusion and invagination suggest changes in membrane curvature induced by +/pho JPs. To better understand the molecular basis of the membrane disruption induced by particles, we quantified lipid packing of membranes upon interaction with particles using fluorescence lifetime imaging microscopy (FLIM). We used C6-NBD-PC as the lipid probe, because the fluorescence lifetime of NBD is known to be highly dependent on its exposure to water.[60] NBD dyes in more disordered lipid membranes are expected to have shortened fluorescence lifetime because they undergo more dynamic quenching from forming hydrogen bonds with water molecules that penetrate the hydrophobic core of the bilayer. We prepared DOPC GUVs containing 1 mol% C6-NBD-PC and acquired spatially resolved lifetime results in the presence of 40 pM +/pho JPs, using FLIM imaging with time-correlated single photon counting. After collecting fluorescence images of GUVs showing membrane protrusions (Fig. 3a), we separated parts of vesicle membranes that showed obvious particle-binding and membrane protrusions from areas with no particle association on the same GUVs and compared their fluorescence lifetimes. Because the lifetime result can vary slightly from one GUV to another, the comparison of different membrane regions on the same GUVs allowed us to identify the effect of particle binding on the C6-NBD-PC lifetime without potential influence from the vesicle-to-vesicle variation effect. Decay curves of photons from pixels within the representative particle-bound membrane area (Fig. 3b) and in the area without particles (Fig. 3c) were each fitted with a two-exponential decay function, where the second lifetime component, τ_2, is sensitive to membrane hydration and therefore the lipid ordering.[48] Histograms of fluorescence lifetimes were also obtained from fitting the decay curve of photons from individual pixels (Fig. 3b and c). It is clear from the histogram that one can see that the lifetime τ_2 of C6-NBD-PC is shorter in the particle-associated membrane protrusions (6.65 ± 0.05 ns) than that in areas without particles (6.87 ± 0.06 ns), while τ_1 remains largely unchanged at around 1.7 ns regardless of the membrane area analyzed. After we mapped the value of τ_2 over the entire GUVs, we confirmed that τ_2 in the GUV membrane is highly heterogeneous and that shorter lifetime τ_2 is correlated with the presence of membrane protrusions where +/pho JPs bound (Fig. 3d). To confirm the generality of this observation, we analyzed and compared τ_2 from membrane areas

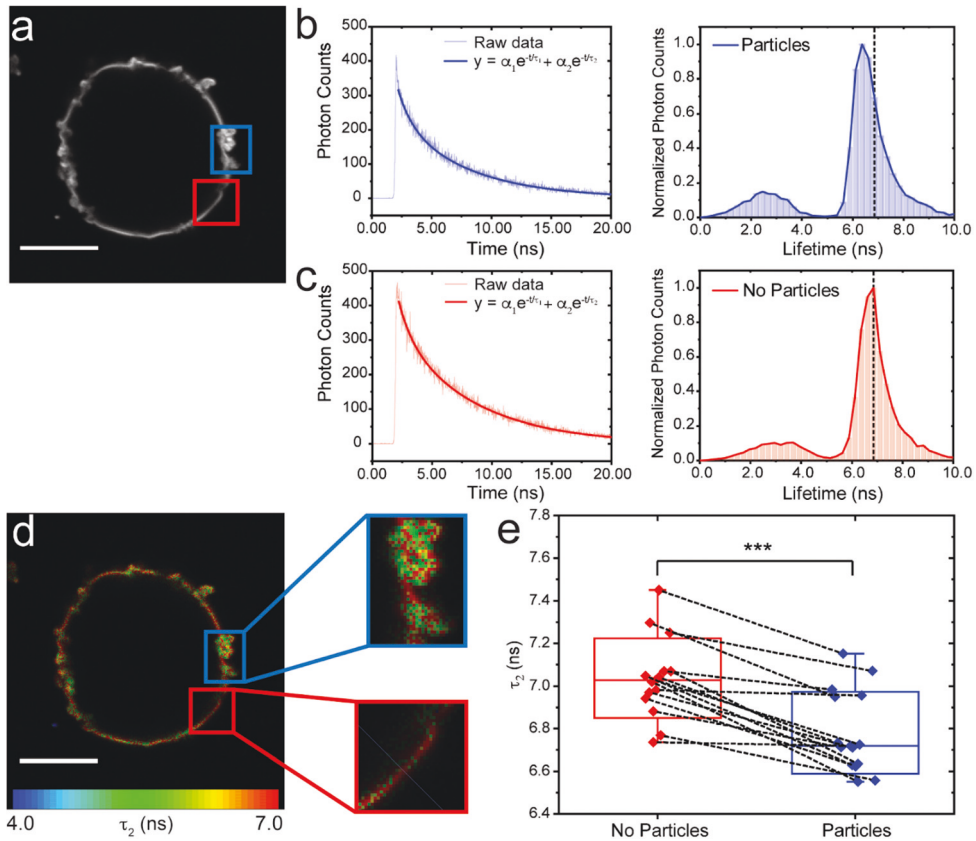

Fig. 3 Fluorescence lifetime microscopy (FLIM) results of GUVs containing lipid probe C6-NBD-PC. (a) A fluorescence image of a GUV incubated with 40 pM +/pho JP. (b and c) Photon decay curve (left) and histogram of fluorescence lifetimes (right) obtained from particle-associated membrane protrusions (b, blue) and undisturbed areas (c, red), which are marked in (a). (d) A FLIM image of a GUV color-coded based on the fluorescence lifetime component τ_2. Insets are zoomed-in FLIM images of the two marked membrane areas: particle-associated membrane protrusions (marked in blue) and undisturbed membrane area (marked in red). (e) Scattered data plot showing τ_2 from undisturbed areas (red) and membrane protrusions (blue) from individual GUVs. Results from each same vesicle are connected by dashed lines. Each box plot indicates the maximum and minimum (short horizontal lines), median (horizontal line), and one standard deviation (box). Statistical significance is noted by *P* values (from Student's *t* test) as follows: ***$P < 0.001$. Scale bars: 15 μm.

with and without bound +/pho JPs in 15 GUVs. As shown in Fig. 3e, in which values of τ_2 from areas in the same GUVs were connected with dashed lines, we confirmed that τ_2 was shorter for particle-bound membrane protrusions compared to areas without particle in all 15 GUVs examined. The extent of the τ_2 decrease varies among different GUVs, which is likely a result of a heterogeneous distribution of particles interacting with the GUVs. Averaged over all 15 GUVs, τ_2 of the membrane areas without bound +/pho JPs was 7.0 ± 0.2 ns, which agrees well with previously reported values in DOPC GUVs.[48] In contrast, τ_2 of particle-bound membrane areas was 6.8 ± 0.2 ns on average. Because the decreased lifetime τ_2 of C6-NBD-PC is known a result of increased penetration of water into the hydrophobic membrane core,[61] our results indicate that the lipid packing is disrupted in the membrane protrusions induced by +/pho JPs. The perturbance of the particles on the lipid ordering is a local effect confined to areas with particle association. It is plausible that +/pho JPs disrupt the lipid packing by inserting the hydrophobic alkyl chains on the gold-coated hemispheres into the vesicle membranes, in a similar mechanism as in the case of +/pho JP disruption to glass-supported lipid bilayers.[46]

Amphiphilic nanoparticle simulations with planar lipid membranes

To further understand the interaction mechanism between the amphiphilic Janus nanoparticle and lipid membrane, we performed molecular dynamics (MD) simulations. To explore the local disruption of the lipid membranes in experiments, the interactions between Janus nanoparticles and a planar lipid membrane was first investigated by using the standard MARTINI coarse-grained (CG) force field.[49–51,54] Our simulations confirm that the hydrophobic part of the amphiphilic nanoparticle is the key to compress and disrupt the lipid membrane. Furthermore, the interaction behaviors of Janus amphiphilic nanoparticles are drastically different from those of the uniform amphiphilic nanoparticles. Firstly, we considered the situation of a single amphiphilic nanoparticle and found that its interaction with the lipid membrane is highly dependent on the particle orientation (Fig. 4a). When the hydrophobic

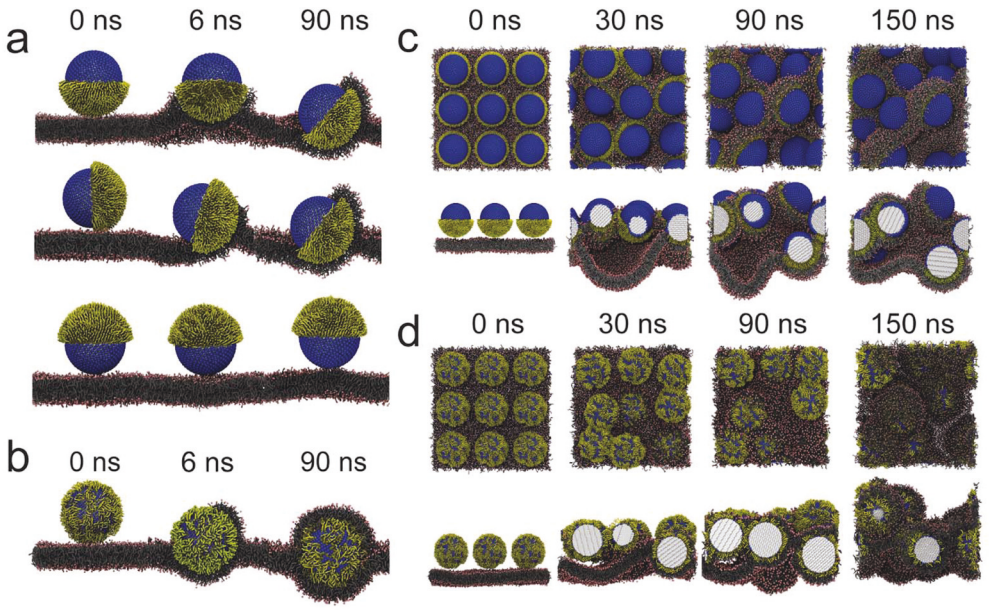

Fig. 4 Molecular simulations on interactions between amphiphilic nanoparticles and a planar lipid membrane. (a) Disruption of lipid membranes by an amphiphilic Janus nanoparticle (+/pho JP) under different orientations. (b) Membrane wrapping of one amphiphilic uniform nanoparticle (+pho UNP). (c) Membrane wrinkling resulted from nine Janus nanoparticles binding to a lipid membrane. (d) Membrane wrapping of nine amphiphilic uniform nanoparticles. Upper and lower panels in (c) and (d) are the top and side view at the simulation time indicated. Size of the lipid membrane in panels a and b is (22 × 22) nm^2 and (42 × 42) nm^2 in panels c and d. The hydrophobic alkyl chains are shown in yellow, the hydrophilic positive beads are colored in blue, and the nanoparticle core is colored in white. Solvent molecules are not shown for clarity.

hemisphere is initially pointing to the lipid membrane, the Janus nanoparticle quickly inserts into the membrane and interacts with lipid tails within a few nanoseconds. The membrane protrudes such that lipids wrap around the hydrophobic hemisphere of the Janus nanoparticle. Eventually, the Janus nanoparticle adheres to the lipid membrane with its entire hydrophobic hemisphere covered by the lipid tails. Additionally, as shown in Fig. 4a, the equilibrated structure of the Janus nanoparticle has a preferred angle on the lipid membrane. This equilibrated structure does not change when the simulated lipid membrane size was increased (Fig. S4†), indicating that the system size in our simulation is large enough to avoid potential artifacts from the periodic boundary conditions. This angle should be a result of the energy balance between hydrophobic interactions, bending energy of the lipid bilayer, and line tension of the lipid edges formed between the hydrophobic and hydrophilic parts of the Janus nanoparticle.[62,63] In contrast, if the hydrophilic hemisphere of the Janus nanoparticle is initially oriented towards the lipid membrane, it does not disrupt the lipid membrane at all. We then performed the simulation with a uniform amphiphilic nanoparticle. Like the Janus nanoparticle case, the lipid membrane also quickly protrudes, and lipids adhere on the uniform amphiphilic nanoparticle, in agreement with our previous findings.[29] However, different from the Janus nanoparticle case, the uniform amphiphilic nanoparticle ends up sandwiched between the two lipid leaflets with its entire surface covered with lipids (Fig. 4b). It is evident that the anisotropic surface chemistry on the Janus nanoparticle changes the mechanism by which amphiphilic nanoparticles disrupt the lipid membrane. From the simulations above, we found that the predominant orientation of +/pho JPs is when their hydrophobic hemisphere initially faces the lipid membrane. Therefore, we next chose this particle orientation to study the particle effect on lipid membrane morphology.

After modeling the interaction between a single Janus nanoparticle with lipid membrane, we moved forward to investigate the situation of multiple nanoparticles. Here, we push the simulation limit to a high nanoparticle density at around 5000 nanoparticles/μm^2. Additionally, the hydrophobic hemisphere of the Janus particle is initially oriented towards the lipid membrane to facilitate their interactions. The individual particles interact with the membrane the same way: the lipid membrane protrudes and wraps around the hydrophobic hemisphere of the Janus nanoparticles. However, the multiple Janus nanoparticles also are attracted to one another through their hydrophobic hemispheres, due to their high density (Fig. 4c). Because of the inter-particle attraction, these nanoparticles are driven to aggregate together with their hydrophilic hemispheres pointing towards outside. This aggregation of particles causes effective compressive stress to squeeze the lipid bilayer, resulting in the "wrinkling" of the lipid bilayer. In contrast, the uniform amphiphilic nanoparticles are "sandwiched" between the two lipid leaflets by the lipid bilayer and do not cause membrane wrinkling (Fig. 4d). Additionally, we compared the projected area of the lipid membrane during the interaction process shown in Fig. 4c and d. We found that the membrane wrinkling caused by the Janus nanoparticles leads

to more membrane compression compared to the membrane insertion of uniform nanoparticles (Fig. S5†).

Amphiphilic Janus nanoparticle simulations with lipid vesicles

We further investigated the global effect of multiple Janus nanoparticles on the vesicle membrane and how it might depend on the spatial distribution of the nanoparticles. Here, the dry MARTINI force field was used.[54] By excluding water molecules, we were able to simulate a lipid vesicle of around 80 nm in diameter with different amount of nanoparticles on the vesicle surface. We considered three different concentrations with 5, 10, and 15 Janus nanoparticles uniformly separated over the entire vesicle surface, respectively (Fig. 5a). Because the local density of nanoparticles on the vesicle is relatively low in all three cases compared to the planar bilayer case, the inter-particle interaction is weak. Our simulation shows that all Janus nanoparticles eventually insert their hydrophobic hemisphere into the lipid vesicle membrane. To quantitatively show the compressive effect of the Janus particles on the vesicles, we calculated the vesicle radius in the simulation as $R = \left[\frac{1}{N}\sum_{i=1}^{N}(r_i - r_{COM})^2\right]^{1/2}$, where N is the total number of lipid molecules in the vesicle, r_i is the center of mass for a lipid molecule, and r_{COM} is the center of mass for the lipid vesicle. We found that the lipid vesicle decreases in size with time during the simulation, indicating that the Janus particles collectively compress the lipid vesicle (Fig. 5b). Furthermore, this global compressive stress is more pronounced when the Janus nanoparticle concentration increases, which is consistent with our experimental results.

We further investigated how the spatial distribution of Janus nanoparticle on the vesicle surface influences their global compressive effect on the membrane. We considered two cases: a total of 10 Janus nanoparticles are uniformly separated over the entire vesicle surface in one case, but unevenly distributed to only one side of the vesicles in the other case (Fig. S6a†). Our simulations show that the global compressive stress exerted on vesicle membranes is more pronounced when the Janus nanoparticles are uniformly distributed over the vesicle surface, as shown by the result that the vesicle shrinks more in size in this case compared to the case with unevenly distributed nanoparticles (Fig. S6b†). This shows that the way the Janus nanoparticles are spatially distributed on the vesicle surface influences their global compressive effect on the membrane and subsequently the degree of vesicle deformation.

We should emphasize that the simulation results of lipid vesicles and planar lipid bilayers confirm our experimental observations from different aspects of the Janus nanoparticle–membrane interactions. In the planar lipid membrane simulations, the local concentration of Janus nanoparticles is exceptionally high due to the periodic boundary conditions. The results demonstrate what happens when the local concentration of Janus nanoparticles is high on membranes. In this case, the amphiphilic Janus nanoparticles induce local membrane wrinkling when nanoparticles are driven to coalesce by the inter-particle hydrophobic interactions. Experimentally, we indeed observed the membrane wrinkling, budding, and invagination in some, but not all, vesicles (Fig. 2). On the other hand, simulations of the lipid vesicle interacting with multiple Janus nanoparticles address the global membrane compression effect from the overall spatial distribution of the nanoparticles. In this simulation, the local concentration of these nanoparticles is relatively low. The interactions between these nanoparticles are weak as they are far away from each other and can move around on the vesicle. Thus, the vesicle membrane deforms locally due to the wrapping and bending around individual nanoparticles. This local membrane deformation is transformed collectively into compressive stress due to the volume-area constraint of the vesicle. Such global membrane compression is most pronounced when the nano-

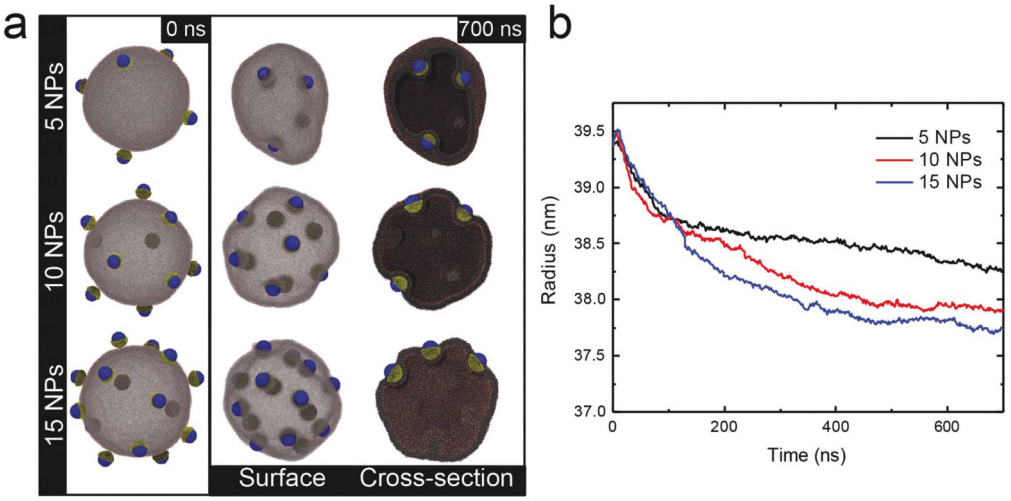

Fig. 5 Molecular simulations on interactions between Janus nanoparticles and a lipid vesicle. (a) Janus nanoparticles at different concentrations bind to a lipid vesicle. (b) Changes in the vesicle radius as a function of simulation time.

particles are uniformly distributed over the vesicle surface, with the concentration of nanoparticles increasing.

Conclusions

In this study, we combined experiments and coarse-grained molecular simulations to investigate the impact of amphiphilic Janus nanoparticles on the morphology and structural integrity of giant unilamellar vesicles made of zwitterionic lipids. These Janus nanoparticles are hydrophobic on one hemisphere and cationic on the other. Unlike our previous work on the interaction of such particles with glass-supported lipid bilayers,[45–47] we focused on giant lipid vesicles in this study, which are better mimics of the cell plasma membrane. Compared to glass-supported lipid bilayers, vesicle membranes are free of the potential influences from the underlying solid substrates but have their unique volume-surface area constraints. We postulated that, as a result of those differences, the giant vesicles are expected to undergo shape instabilities differently than lipid bilayers upon the same interactions with Janus nanoparticles. Indeed, we demonstrated here that amphiphilic Janus nanoparticles disrupted the structural integrity and induced morphological deformations in giant lipid vesicles that were not observed in planar supported lipid bilayers. Binding of Janus nanoparticles was found to induce membrane "wrinkling" characteristic of high local curvatures and, in some cases, membrane protrusions and budding. The "wrinkled" membrane areas are more disordered in lipid packing compared to areas without particle association. We demonstrated in molecular simulations that amphiphilic Janus nanoparticles insert into the lipid membrane and cause local structural disorders for membrane wrapping around the hydrophobic hemisphere of Janus nanoparticles. When a few of such membrane-particle interaction events take place adjacent to one another, the nanoparticles collectively compress the vesicle membrane laterally and induce membrane wrinkling. Importantly, we show that interaction from multiple nanoparticles with the same lipid vesicle can generate a collective compressive stress on the membrane, which becomes most pronounced when the nanoparticles are uniformly distributed over the entire vesicle surface.

Aside from unique shape changes of giant vesicles induced by amphiphilic Janus nanoparticles, there are some similarities between the vesicle and the glass-supported lipid bilayer systems. First, we found that the threshold particle concentration needed to disrupt vesicle membrane integrity is 20 pM, the same as that for inducing holes in the glass-supported lipid bilayers. This suggests that the glass substrates underneath a planar bilayer have a negligible influence on the specific interactions that determine the particle threshold concentration. Second, we demonstrated, in both experiments and simulations, that hydrophobic interactions between the amphiphilic Janus nanoparticles and membranes are the major driving force for shape instabilities of the giant vesicles. Last, our results from the giant lipid vesicle system again demonstrate that amphiphilic Janus nanoparticles are more effective than the uniformly mixed particles in disrupting the lipid membranes.

Our findings here, together with our previous studies, present a compelling argument that the impact of nanoparticles on the biological membranes depends on not only the overall surface chemistry of the particles, but also the way chemical groups are spatially arranged on the particle surface. These results highlight the need for broader and more in-depth studies on understanding the role of heterogeneous surface chemistry of nanomaterials in determining their impacts on biological systems.

Conflicts of interest

There are no conflicts to declare.

Acknowledgements

We thank Dr Giovanni Gonzalez-Gutierrez at IUB Physical Biochemistry Instrumentation Facility and Dr Jim Powers at IUB Light Microscopy Imaging Center for assistance with instrument use. Fabrication and characterization of Janus particles were done at the IUB Nanoscale Characterization Facility. This work was supported by the National Science Foundation under Grant No. 1705384 to Y. Y. and No. 1755779 to Y. L. Y. L. also acknowledges the Texas Advanced Computing Center (TACC) at The University of Texas at Austin for providing HPC resources (Frontera project and the National Science Foundation award 1818253) that have contributed to the research results reported within this paper.

References

1 A. Verma and F. Stellacci, *Small*, 2010, **6**, 12–21.
2 A. M. Farnoud and S. Nazemidashtarjandi, *Environ. Sci.: Nano*, 2019, **6**, 13–40.
3 Z. Shen, M.-P. Nieh and Y. Li, *Polymers*, 2016, **8**, 83.
4 Y. Li, M. Kröger and W. K. Liu, *Biomaterials*, 2014, **35**, 8467–8478.
5 P. R. Leroueil, S. A. Berry, K. Duthie, G. Han, V. M. Rotello, D. Q. McNerny, J. R. Baker Jr., B. G. Orr and M. M. Banaszak Holl, *Nano Lett.*, 2008, **8**, 420–424.
6 S. Li and N. Malmstadt, *Soft Matter*, 2013, **9**, 4969–4976.
7 J. Lin, H. Zhang, Z. Chen and Y. Zheng, *ACS Nano*, 2010, **4**, 5421–5429.
8 H. Lee and R. G. Larson, *J. Phys. Chem. B*, 2008, **112**, 12279–12285.
9 H. Lee and R. G. Larson, *J. Phys. Chem. B*, 2008, **112**, 7778–7784.
10 H. Lee and R. G. Larson, *J. Phys. Chem. B*, 2006, **110**, 18204–18211.
11 A. Mecke, S. Uppuluri, T. M. Sassanella, D.-K. Lee, A. Ramamoorthy, J. R. Baker, B. G. Orr and M. M. Banaszak Holl, *Chem. Phys. Lipids*, 2004, **132**, 3–14.

12 S. Zuraw-Weston, D. A. Wood, I. K. Torres, Y. Lee, L.-S. Wang, Z. Jiang, G. R. Lázaro, S. Wang, A. A. Rodal, M. F. Hagan, V. M. Rotello and A. D. Dinsmore, *Nanoscale*, 2019, **11**, 18464–18474.
13 Y. Yu and S. Granick, *J. Am. Chem. Soc.*, 2009, **131**, 14158–14159.
14 J.-Q. Lin, Y.-G. Zheng, H.-W. Zhang and Z. Chen, *Langmuir*, 2011, **27**, 8323–8332.
15 B. Wang, L. Zhang, S. C. Bae and S. Granick, *Proc. Natl. Acad. Sci. U. S. A.*, 2008, **105**, 18171.
16 A. Gupta, R. F. Landis, C.-H. Li, M. Schnurr, R. Das, Y.-W. Lee, M. Yazdani, Y. Liu, A. Kozlova and V. M. Rotello, *J. Am. Chem. Soc.*, 2018, **140**, 12137–12143.
17 X. Li, S. M. Robinson, A. Gupta, K. Saha, Z. Jiang, D. F. Moyano, A. Sahar, M. A. Riley and V. M. Rotello, *ACS Nano*, 2014, **8**, 10682–10686.
18 P. Chen, Z. Xu, G. Zhu, X. Dai and L.-T. Yan, *Phys. Rev. Lett.*, 2020, **124**, 198102.
19 P. U. Atukorale, Z. P. Guven, A. Bekdemir, R. P. Carney, R. C. Van Lehn, D. S. Yun, P. H. Jacob Silva, D. Demurtas, Y.-S. Yang, A. Alexander-Katz, F. Stellacci and D. J. Irvine, *Bioconjugate Chem.*, 2018, **29**, 1131–1140.
20 C.-F. Su, H. Merlitz, H. Rabbel and J.-U. Sommer, *J. Phys. Chem. Lett.*, 2017, **8**, 4069–4076.
21 H.-Y. Lee, S. H. R. Shin, L. L. Abezgauz, S. A. Lewis, A. M. Chirsan, D. D. Danino and K. J. M. Bishop, *J. Am. Chem. Soc.*, 2013, **135**, 5950–5953.
22 P. U. Atukorale, Y.-S. Yang, A. Bekdemir, R. P. Carney, P. J. Silva, N. Watson, F. Stellacci and D. J. Irvine, *Nanoscale*, 2015, **7**, 11420–11432.
23 P. Chen, H. Yue, X. Zhai, Z. Huang, G.-H. Ma, W. Wei and L.-T. Yan, *Sci. Adv.*, 2019, **5**, eaaw3192.
24 B. Jing, R. C. T. Abot and Y. Zhu, *J. Phys. Chem. B*, 2014, **118**, 13175–13182.
25 B. Jing and Y. Zhu, *J. Am. Chem. Soc.*, 2011, **133**, 10983–10989.
26 S. H. R. Shin, H.-Y. Lee and K. J. Bishop, *Angew. Chem., Int. Ed.*, 2015, **54**, 10816–10820.
27 R. C. Van Lehn and A. Alexander-Katz, *PLoS One*, 2019, **14**, e0209492.
28 R. C. Van Lehn and A. Alexander-Katz, *Soft Matter*, 2015, **11**, 3165–3175.
29 Z. Shen, W. Baker, H. Ye and Y. Li, *Nanoscale*, 2019, **11**, 7371–7385.
30 K. An and G. A. Somorjai, *ChemCatChem*, 2012, **4**, 1512–1524.
31 S. Cheong, J. D. Watt and R. D. Tilley, *Nanoscale*, 2010, **2**, 2045–2053.
32 C.-J. Zhong, J. Luo, P. N. Njoki, D. Mott, B. Wanjala, R. Loukrakpam, S. Lim, L. Wang, B. Fang and Z. Xu, *Energy Environ. Sci.*, 2008, **1**, 454–466.
33 G. R. Aiken, H. Hsu-Kim and J. N. Ryan, *Environ. Sci. Technol.*, 2011, **45**, 3196–3201.
34 A. J. Edgington, A. P. Roberts, L. M. Taylor, M. M. Alloy, J. Reppert, A. M. Rao, J. Mao and S. J. Klaine, *Environ. Toxicol. Chem.*, 2010, **29**, 2511–2518.
35 Q. Fang, Q. Shi, Y. Guo, J. Hua, X. Wang and B. Zhou, *Environ. Sci. Technol.*, 2016, **50**, 1005–1013.
36 J. Yan, B. Lin, C. Hu, H. Zhang, Z. Lin and Z. Xi, *Nanoscale Res. Lett.*, 2014, **9**, 406.
37 S. P. Yang, O. Bar-Ilan, R. E. Peterson, W. Heideman, R. J. Hamers and J. A. Pedersen, *Environ. Sci. Technol.*, 2013, **47**, 4718–4725.
38 P. Gkeka, L. Sarkisov and P. Angelikopoulos, *J. Phys. Chem. Lett.*, 2013, **4**, 1907–1912.
39 Y. Li, X. Li, Z. Li and H. Gao, *Nanoscale*, 2012, **4**, 3768–3775.
40 A. Verma, O. Uzun, Y. Hu, Y. Hu, H.-S. Han, N. Watson, S. Chen, D. J. Irvine and F. Stellacci, *Nat. Mater.*, 2008, **7**, 588–595.
41 Q. K. Ong and F. Stellacci, *PLoS One*, 2015, **10**, e0135594.
42 J. Stirling, I. Lekkas, A. Sweetman, P. Djuranovic, Q. Guo, B. Pauw, J. Granwehr, R. Lévy and P. Moriarty, *PLoS One*, 2014, **9**, e108482.
43 H.-M. Ding and Y.-Q. Ma, *Nanoscale*, 2012, **4**, 1116–1122.
44 A. Alexeev, W. E. Uspal and A. C. Balazs, *ACS Nano*, 2008, **2**, 1117–1122.
45 K. Lee and Y. Yu, *Soft Matter*, 2019, **15**, 2373–2380.
46 K. Lee, L. Zhang, Y. Yi, X. Wang and Y. Yu, *ACS Nano*, 2018, **12**, 3646–3657.
47 K. Lee and Y. Yu, *Langmuir*, 2018, **34**, 12387–12393.
48 M. Stöckl, A. P. Plazzo, T. Korte and A. Herrmann, *J. Biol. Chem.*, 2008, **283**, 30828–30837.
49 S. J. Marrink, H. J. Risselada, S. Yefimov, D. P. Tieleman and A. H. de Vries, *J. Phys. Chem. B*, 2007, **111**, 7812–7824.
50 S. J. Marrink, A. H. de Vries and A. E. Mark, *J. Phys. Chem. B*, 2004, **108**, 750–760.
51 S. J. Marrink and D. P. Tieleman, *Chem. Soc. Rev.*, 2013, **42**, 6801–6822.
52 H. Sharma and E. E. Dormidontova, *ACS Nano*, 2017, **11**, 3651–3661.
53 J. Lin, H. Zhang, V. Morovati and R. Dargazany, *J. Colloid Interface Sci.*, 2017, **504**, 325–333.
54 C. M. Arnarez, J. J. Uusitalo, M. F. Masman, H. I. Ingólfsson, D. H. De Jong, M. N. Melo, X. Periole, A. H. De Vries and S. J. Marrink, *J. Chem. Theory Comput.*, 2015, **11**, 260–275.
55 S. Plimpton, *J. Comput. Phys.*, 1995, **117**, 1–19.
56 W. Humphrey, A. Dalke and K. Schulten, *J. Mol. Graphics*, 1996, **14**, 33–38.
57 S. A. Wheaten, A. Lakshmanan and P. F. Almeida, *Biophys. J.*, 2013, **105**, 432–443.
58 E. Poli, K. H. Jong and A. Hassanali, *Nat. Commun.*, 2020, **11**, 901.
59 L. Portilla and M. Halik, *ACS Appl. Mater. Interfaces*, 2014, **6**, 5977–5982.
60 H. A. L. Filipe, Š. Pokorná, M. Hof, M. Amaro and L. M. S. Loura, *Phys. Chem. Chem. Phys.*, 2019, **21**, 1682–1688.
61 G. M'Baye, Y. Mély, G. Duportail and A. S. Klymchenko, *Biophys. J.*, 2008, **95**, 1217–1225.
62 Z. Shen, H. Ye, M. Kröger, S. Tang and Y. Li, *Nanoscale*, 2019, **11**, 15971–15983.
63 Z. Shen, H. Ye, X. Yi and Y. Li, *ACS Nano*, 2019, **13**, 215–228.

